Earth's Top-of-Atmosphere Radiation Budget

NG Loeb, W Su, DR Doelling, T Wong, and P Minnis, NASA Langley Research Center, Hampton, VA, United States
S Thomas and WF Miller, Science Systems and Applications, Inc., Hampton, VA, United States

Introduction

Climate change involves a perturbation to Earth's energy budget, which in turn impacts Earth's water cycle. Changes in the composition of the atmosphere either through natural or anthropogenic sources alter how energy is distributed and can lead to irreversible changes in regional climate. At the top-of-atmosphere (TOA), the Earth's energy budget involves a balance between how much solar energy Earth absorbs and how much terrestrial thermal infrared radiation is emitted to space. Since only radiative energy is involved, this is also referred to as Earth's radiation budget (ERB). Approximately 30% of the incident solar radiation reaching Earth is scattered back to space by air molecules, clouds, the Earth's surface, and aerosols. The remaining 70% is absorbed by the surface-atmosphere system, providing the energy necessary to sustain life on Earth. The absorbed solar radiation (ASR) is converted into different forms of energy (e.g., potential, internal, latent, and kinetic energy), and transported and stored throughout the system. The Earth also emits thermal infrared radiation to space as outgoing longwave radiation, which must balance ASR in an equilibrium climate.

When the climate system is forced by natural or anthropogenic factors (e.g., changes in solar output, volcanic eruptions, and human activities), an imbalance in the TOA ERB results. Superimposed on this climate change signal is the large internal variability of the climate system, which also causes variations in the ERB. Internal variations can occur over a range of time-space scales, associated with weather events, atmosphere–ocean interactions [e.g., El Niño-Southern Oscillation (ENSO)], volcanic eruptions, and low-frequency multidecadal fluctuations [e.g., Pacific Decadal Oscillation (PDO)].

Satellite observations of ERB provide critical information needed to better understand the driving mechanisms of climate change. In an excellent review of the history of satellite missions and measurements of ERB, House et al. (1986) note that ERB instruments were amongst the first to fly aboard the early satellite missions of the late 1950s and the 1960s alongside scanning multichannel radiometers used for weather research and prediction. In conjunction with ERB instrument improvements, there has also been a steady improvement in the algorithms used to interpret the satellite measurements and scientific analyses of ERB and its role in climate. In the 1960s, the first instrument model describing radiometric performance for processing Explorer 7 data was developed (Weinstein and Suomi, 1961), and the first models for converting satellite measurements to radiative fluxes were applied that did not assume Earth targets to be Lambertian (Arking and Levine, 1967). During the late 1960s and the 1970s, the medium- and high-resolution infrared radiometer (Raschke and Bandeen, 1970; Raschke et al., 1973) instruments aboard the Nimbus satellites provided the first global measurements of the ERB and the first estimates of an average flux over a 24-h period, which is needed to compute detailed estimates of ERB components regionally and by season (Raschke et al., 1973). The Nimbus 7 mission

provided the first continuous long-term calibrated observations of the ERB with a nonscanner wide field-of-view instrument, spanning from 1978 to 1987 (Kyle, 1990). Another instrument on Nimbus 7 consisted of biaxial scanning telescopes to observe angular distribution of SW and LW radiances. These data were used to develop the first empirical angular models for converting observed radiances into radiative fluxes (Suttles et al., 1988; Taylor and Stowe, 1984). During the Earth radiation budget satellite experiment (ERBE), many other advances in instrument calibration and algorithms for processing ERB data were developed (Barkstrom, 1984).

This article provides an overview of global ERB data products and algorithms generated by the Clouds and the Earth's Radiant Energy System (CERES) project. CERES produces ERB data products at multiple levels from the TOA to the surface, but we focus here on TOA only and refer to papers by Rose et al. (2013), Rutan et al. (2015), and Kato et al. (2013) for further information about CERES surface radiation products. A key advance of CERES over previous ERB datasets is extensive use of coincident higher spatial resolution spectral imager measurements on both low-Earth orbit and geostationary platforms. These instruments enable a host of other variables describing cloud, aerosol and surface properties to be retrieved alongside CERES radiative fluxes. CERES has an integrated instrument/algorithm/validation science team that is responsible for monitoring the health of the CERES sensors, provide calibrated radiances (Level 1) and instantaneous (Level 2) and temporally and spatially averaged (Level 3) data products, perform validation, and enable scientific investigations using the CERES data. The CERES climate data records (CDRs) account for the regional and global diurnal cycle of radiative fluxes and include coincident cloud, aerosol, surface, and meteorological properties so that changes in the ERB and climate system components can be investigated in an integrated manner. Accomplishing this objective requires a high level of data fusion involving 13 instruments on 8 spacecraft, all integrated to obtain climate accuracy in radiative fluxes from the top to the bottom of the atmosphere. A total of 25 unique input data sources are used to produce 18 CERES data products. Over 90% of the CERES data product volume involves two or more instruments, and individual data products include up to 260 unique parameters.

Fig. 1 provides the CERES data processing flow diagram, listing the algorithm steps and ancillary input data needed to produce the CERES TOA radiation data products. The CERES data products are divided into processing levels, defined in **Table 1**. In the following sections we will describe the CERES instruments, their calibration, and briefly discuss the algorithm steps and ancillary input data used to produce the CERES data products.

CERES Instruments

The CERES instrument (**Fig. 2**) is a 3-channel scanning radiometer that uses precision thermistor bolometer detectors to observe radiation between 0.3 and 200 μm (total channel), 0.3 and 5 μm (shortwave channel), and 8 and 12 μm (window channel) (Wielicki et al., 1996). **Table 2** provides the instrument characteristics for CERES instruments aboard the tropical rainfall measuring mission (TRMM), Terra, Aqua, and Suomi National Polar-orbiting Partnership (S-NPP) satellites. Each channel has a Cassagrain telescope that houses the detector, primary and secondary mirrors, and forward and rear filters (**Fig. 3**). The detector lies behind a hexagonal field stop that determines the $1.3^\circ \times 2.6^\circ$ field-of-view (FOV), which is approximately a factor of 2 smaller than ERBE. The three CERES telescopes are coaligned so that they have a 98% common FOV. The mirrors are silver coated, providing spectrally flat response functions, except between 0.3 and 0.4 μm, where there is a sharp decrease in spectral response. Because the CERES scanning radiometer has a finite response time, it has a point-spread function (PSF) that describes the response of the radiometer to a point source of radiation from a given direction (Smith, 1994). The PSF characteristics are determined by the shape of the field stop, time response of the detector (8 ms), and signal conditioning circuit.

The CERES channels are coaligned and mounted on a spindle that rotates about the elevation axis. Every CERES scan takes 6.6 s and involves a scan from space beyond the Earth limb, across the Earth to space on the opposite side, a pause at the internal calibration source, and a scan back across the Earth to space on the other side (Wielicki et al., 1996). CERES instruments can be commanded from the ground to scan in different modes. In cross-track mode, the scan is perpendicular to the ground track so that spatial sampling is optimized, providing global coverage daily. This is the primary mode used to produce CERES Level-3 gridded data products. The CERES rotating azimuth plane (RAP) scan mode relies on the instrument's azimuthal axis drive system to optimize angular sampling. When in RAP mode, the instrument scans in elevation as it rotates in azimuth, thereby acquiring radiances over a range of viewing zenith and relative azimuth angle combinations. CERES RAP data are needed to construct CERES angular distribution models (ADMs), described in "**Radiance-to-Flux Conversion**" section . CERES can also be placed in along-track mode to acquire measurements of a target from multiple viewing zenith angles. Finally, in the programmable azimuth plane mode, the CERES angular sampling is commanded from the ground by uploading instructions to the instrument to acquire multiangle measurements for specific scientific experiments (e.g., field campaigns, intercalibration with other instruments, etc.).

Instrument Calibration

Ground Calibration

Prior to launch, the CERES instruments underwent extensive ground calibration at a radiometric calibration facility (RCF) located at Northrop Grumman Aerospace Systems (formerly TRW Space and Technology Group) in Redondo Beach, California (Lee et al., 1998). It is during ground calibration that the CERES instruments are traced to absolute standards. The RCF is a

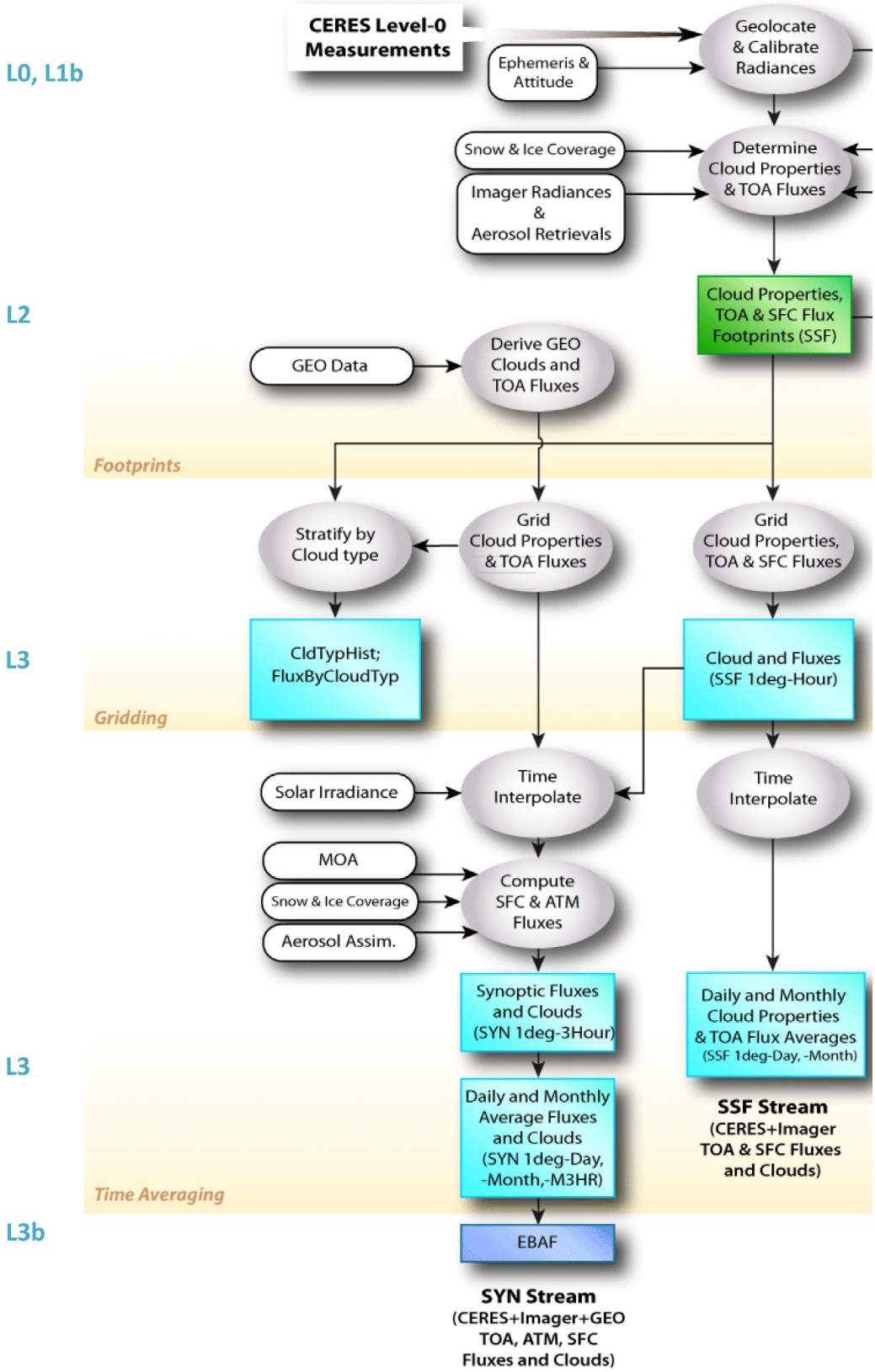

Fig. 1 CERES data processing flow diagram. The colored boxes correspond to different CERES data products, gray boxes denote an algorithm step, and *white* boxes are ancillary data sets.

Table 1 CERES processing level descriptions

Level	*Description*
0	Raw digitized instrument data for all engineering and science data streams
1b	Instantaneous filtered broadband radiances at the CERES footprint resolution, geolocation and viewing geometry, solar geometry, satellite position and velocity, and all raw engineering and instrument status data
2	Instantaneous geophysical variables at the CERES footprint resolution. Includes some Level 1b parameters and retrieved or computed geophysical variables (e.g., filtered and unfiltered radiances, viewing geometry, radiative fluxes, imager cloud, and aerosol properties)
3	Radiative fluxes and cloud properties spatially averaged onto a uniform grid. Includes either instantaneous averages sorted by local/GMT hour (e.g., SSF1deg–Hour) or temporally interpolated averages at 3-hourly, daily, monthly or monthly hourly intervals (e.g., SSF1deg–Month)
3b	Level 3 data products adjusted within their range of uncertainty to satisfy known constraints (e.g., consistency between average global net TOA flux imbalance and ocean heat storage)

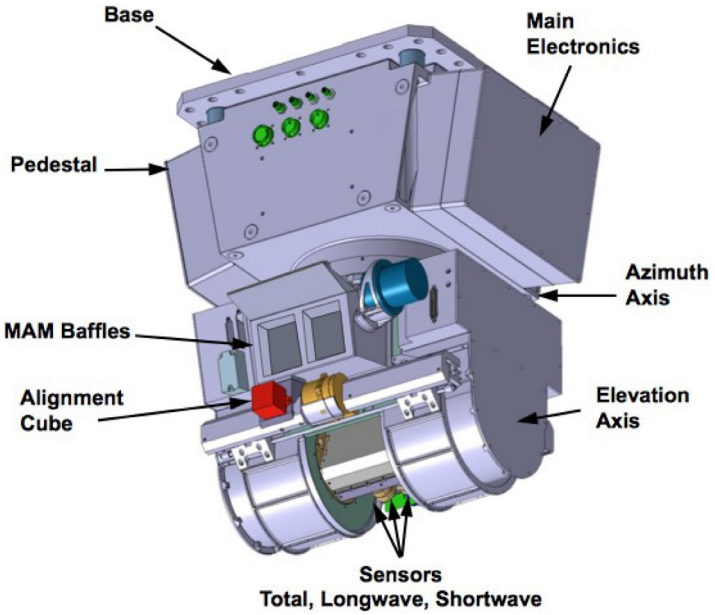

Fig. 2 CERES scanning radiometer.

Table 2 CERES instrument characteristics for TRMM, Terra, Aqua, and S-NPP missions

	TRMM (PFM)	*Terra (FM1, FM2)*	*Aqua (FM3, FM4)*	*S-NPP (FM5)*
Orbit	35 degrees inclination	Sun-synchronous, near polar, 10:30 am descending node	Sun-synchronous, near polar, 1:30 pm ascending node	Sun-synchronous, near polar, 1:30 pm ascending node
Altitude (km)	705	705	705	824
Spatial resolution (km)	10	20	20	24
Spectral channels	Shortwave: 0.3–5.0 μm; Window: 8–12 μm; Total: 0.3–200 μm			
Swath dimensions	Limb to limb			
Angular sampling	Cross-track scan and 360 degrees azimuth biaxial scan			
Duty cycle (%)	100			
Mass (kg)	45			
Power (W)	45			
Data rate (kbps)	10			
Size (cm)	$60 \times 60 \times 70$ (deployed)			
Design life (years)	6			

PFM, proto-flight model; FM, flight model.

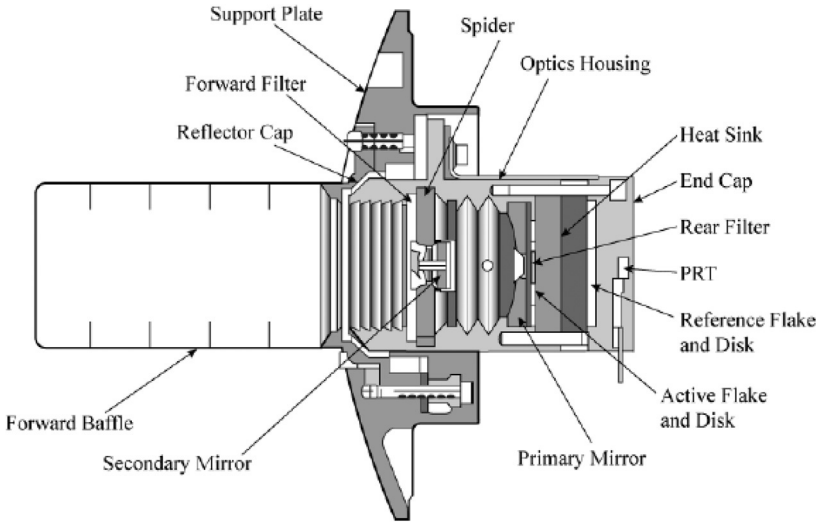

Fig. 3 Cross-section of CERES telescope.

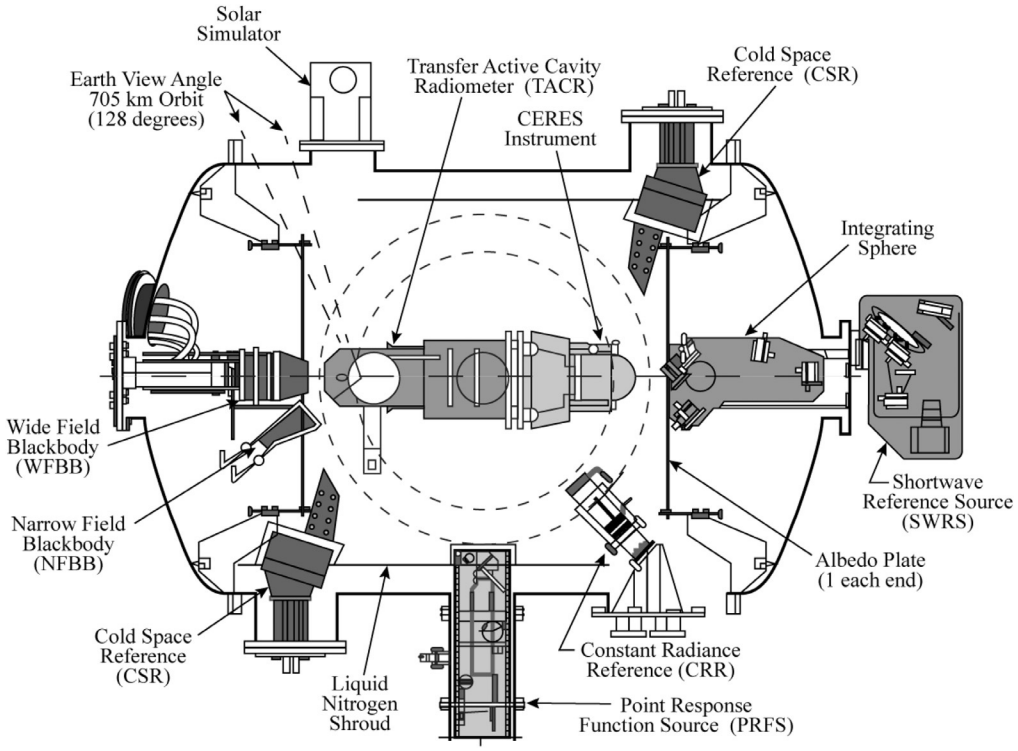

Fig. 4 CERES radiometric calibration facility.

calibration vacuum chamber that simulates the space environment. The CERES instrument is placed on a carousel that can be rotated and moved vertically so that it can be calibrated against different reference sources (Fig. 4). These include cryogenically cooled blackbodies for LW calibration, a SW reference source, a cold space reference source, a PSF measurement source, a constant radiance reference source to test for scan-dependent variations, and a solar simulator to emulate solar calibrations. The absolute calibration for the TOT and WN channels is performed using a narrow field-of-view blackbody, tied to the International Temperature Scale of 1990. The blackbody source along with a transfer active cavity radiometer is used to calibrate the shortwave reference source, which in turn brings the SW channel to the same calibration reference. The sensor responsivity is determined using the onboard sources during the prelaunch calibrations. CERES goals for absolute calibration of radiance are 0.5% for LW and 1% for SW.

In-Flight Calibration Changes

Because all Earth-viewing satellite instruments experience a loss of measurement sensitivity with time (e.g., due to UV exposure, molecular contamination, etc.), the instrument needs to be monitored using a combination of the instrument's onboard calibration subsystem and vicarious calibration methods to detect, quantify and correct for changes in instrument sensitivity throughout the mission so that subtle changes in the climate system can be unambiguously detected. The accuracy and stability of the CERES CDR rests upon the ERB science team's ability to accurately calibrate the instruments and correct for artificial instrument drifts. The primary in-flight calibration systems used to detect drifts in CERES sensor gains are the Internal Calibration Module (ICM) and the Mirror Attenuator Mosaic (MAM) (Lee et al., 1992; Priestley et al., 2000, 2011). The ICM consists of two blackbody calibration sources for the TOT and WN sensors and a shortwave internal calibration source (SWICS) for the SW sensor. The blackbodies operate at temperatures of 295, 305, and 315 K, and are monitored by a platinum-resistance thermometer. The SWICS consists of an evacuated quartz tungsten lamp operating at three discrete current levels producing spectra equivalent to 2100, 1900, and 1700 K brightness temperatures. The radiometers observe the ICM in every normal cross-track elevation scan. Monthly gains are determined from ICM calibrations performed weekly, and a 5-month running mean is used to reduce noise. Fig. 5A–E shows the FM1-FM5 internal calibration results. The total channel response to LW radiation has gradually increased with time for all five instruments. The increases relative to the beginning-of-mission are 0.6% for FM1, 0.7% for FM2, 0.7% for FM3, 1% for FM4, and 0.4% for FM5. The SW channel response changed only slightly for FM1 (<0.1%), while for FM2 the change is approximately −0.4%, and for FM3 it is 0.4%. There was an increase of about 0.6% for the FM4 SW sensor through Apr. 2005, when it failed prematurely. The FM5 SW channel response decreased by 0.2%. The window sensor gains show an increasing trend for four of the instruments except FM3, which shows a decrease with time. These instrument calibration drifts were observed over 13 years and are very small. These calibration drifts are removed when applying the calibration gain.

The MAM is a solar diffuser plate used for calibrating the shortwave sensor and the total sensor. It consists of a baffle to block stray light and a nickel substrate with aluminum coated spherical divots that attenuate and redirect the solar radiation into the FOV of the sensors. For CERES instruments on Terra and Aqua, the MAM coatings degraded in orbit and therefore were not used (Priestley et al., 2011). For S-NPP, the MAMs are performing nominally thus far.

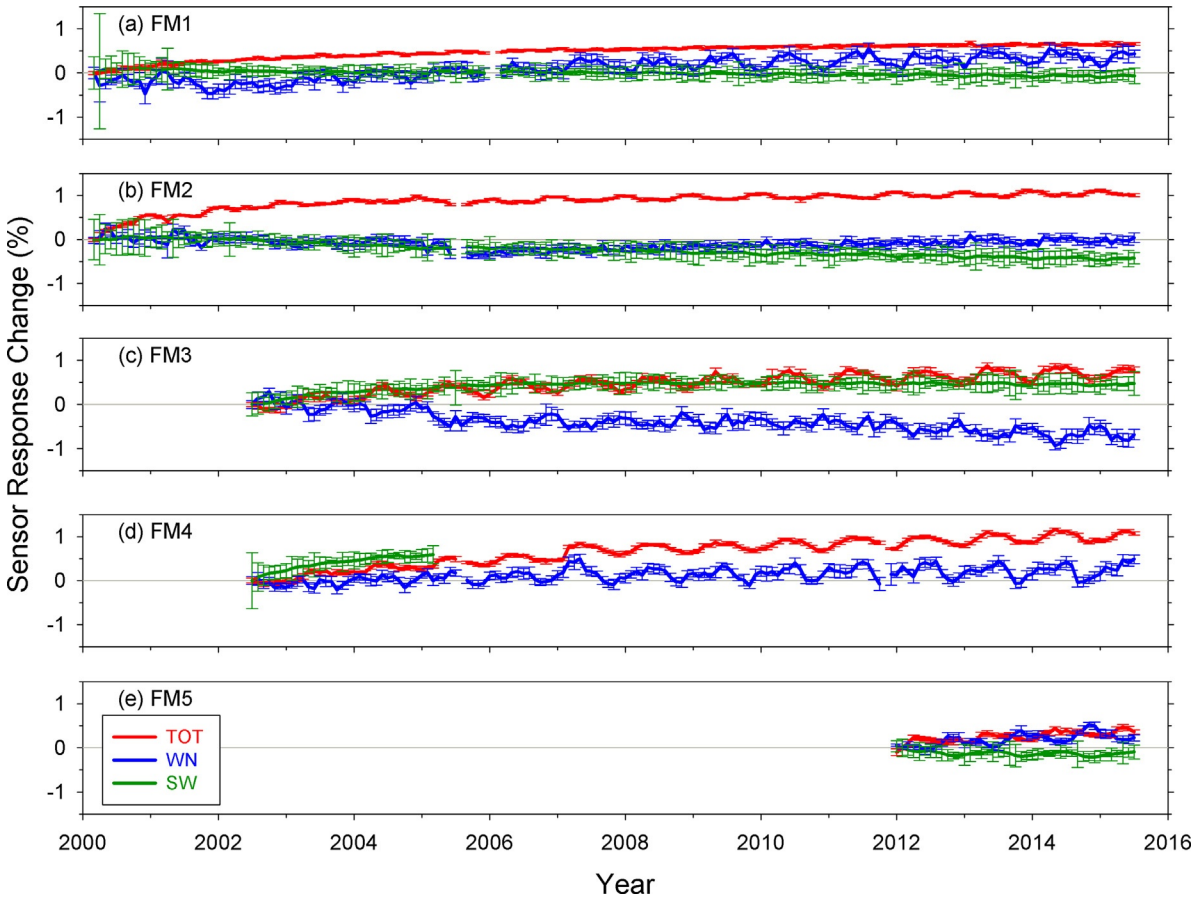

Fig. 5 On-orbit sensor gain trends for CERES FM1—FM5 instruments.

Instantaneous Clouds and Radiation: Single Scanner Footprint Product

Once the CERES measurements have been calibrated, the next step in the CERES processing system (Fig. 1) is to produce the Level-2 single scanner footprint (SSF) data product. The SSF consists of CERES viewing geometry and radiances, TOA and surface radiative fluxes, imager aerosol and cloud properties (see "Imager-Derived Properties" section), surface type information, solar irradiance, and meteorological data from reanalysis. SSF is a key input to higher-level CERES data products and is also extensively used by the research community in process study research (e.g., especially research on aerosol-cloud-radiation interactions). The following sections provide a brief overview of the steps used to create the CERES Level-2 SSF product.

Unfiltered Radiances

The gain coefficients (Fig. 5) convert CERES output voltages from digital counts to filtered radiances, which represent the radiation that is filtered through the instrument optics. To correct for the imperfect spectral response of the instrument, filtered radiances are converted to unfiltered radiances, which correspond to radiation received by the instrument prior to entering the optics. It is the unfiltered radiances that are converted to radiative fluxes in the CERES processing system. The unfiltering process involves applying an algorithm that relates unfiltered and filtered radiances based upon knowledge of the instrument spectral response function (SRF) and a spectral radiance database representative of Earth scenes (Loeb et al., 2001). Shankar et al. (2010) re-evaluated the ground calibration data collected prior to the CERES Terra and Aqua launches and derived new prelaunch gains and SRFs for each CERES instrument using spectral measurements collected using a Fourier Transform Spectrometer system along with the blackbody calibration data. Fig. 6 provides CERES SRFs for the FM1 instrument. The SRFs are spectrally flat over most of the spectrum except between 0.3 and 0.4 μm, where there is a sharp decrease. The shape is characteristic of silver coated primary and secondary mirrors.

Imager-Derived Properties

The availability of imager measurements coincident with CERES helps increase the accuracy of CERES TOA fluxes, improves clear-sky scene identification used in determining cloud radiative effect, enables surface fluxes to be computed, and provides cloud, aerosol and surface skin temperature retrievals for attribution studies involving CERES radiative fluxes. CERES has flown with the Visible and Infrared Scanner on TRMM, the moderate-resolution imaging spectrometer (MODIS) on Terra and Aqua, and the visible/infrared imager/radiometer suite (VIIRS) on S-NPP. Aerosol properties in the CERES SSF are produced at NASA Goddard Space Flight Center based upon (Remer et al., 2008; Levy et al., 2007; Hsu et al., 2004). The algorithms developed for MODIS are now being extended to VIIRS on S-NPP. The CERES team determines cloud properties and surface skin temperatures directly from imager pixel data based upon Minnis et al. (2011). As a radiation budget project, CERES requires cloud retrievals even for the most challenging cases (e.g., near cloud edges, complex multilayer cloud conditions, etc.), which is not a common feature of cloud property datasets (Stubenrauch et al., 2013). CERES cloud algorithm changes are closely coordinated with higher-level data product algorithm changes in order to minimize sudden discontinuities in the CERES record. Also, in order to minimize the effects of algorithm shock, CERES imager-derived properties are designed to work in a consistent manner across multiple platforms (Terra, Aqua, S-NPP, 18 geostationary visible/infrared imagers).

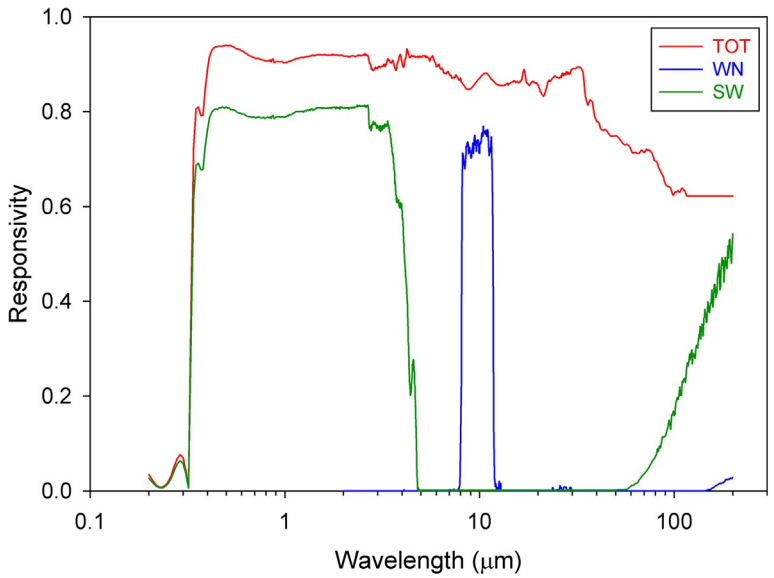

Fig. 6 Spectral response function for CERES sensors.

Pixel imager-based cloud property retrievals include cloud boundaries, phase, optical depth, effective particle size, and condensed/frozen water path. In the latest version of CERES SSF (Edition 4), improvements to the CERES cloud algorithm (Minnis et al., 2010) include the following: changes to the cloud mask that result in better agreement with the Cloud-Aerosol Lidar and Infrared Pathfinder Satellite Observations (CALIPSO); a new ice crystal reflectance model based on rough hexagonal columns; implementation of a combined 1.38-μm reflectance and infrared technique that extends the range of cirrus optical depth retrievals to below 0.3; a multilayer cloud detection and retrieval scheme; new clear-sky and surface albedos for the 0.65, 1.24, and 2.13 μm channels to enable cloud effective radius retrievals in all three channels; a new scheme for improved retrievals of low cloud heights based upon matched MODIS and CALIPSO data (Sun-Mack et al., 2014), new cloud thickness parameterizations from matched MODIS, CALIPSO, and CloudSat data; a new cloud-top-height technique for more accurate height assignments for optically thick ice cloud.

Convolution

Convolution involves the process of merging multiple datasets and averaging them over individual CERES footprints. In order to do this accurately, one must account for the instrument's PSF, which provides the weight each pixel value receives in the averaging process. The PSF of a radiometer describes the response of the radiometer to a pencil of radiance from a given direction (Smith, 1994). For a scanning radiometer, the effect of the time response of the detector on the PSF must be considered when the sampling rate is comparable to the response time of the detector. In addition, the signal is usually filtered electronically prior to sampling in order to attenuate electronic noises and to remove high frequency components of the signal, which would cause aliasing errors. The time responses of the detector and filter cause a lag in the output relative to the input radiance, so that the time response causes the centroid of the PSF to be displaced from the centroid of the optical FOV (Fig. 7). In addition, the time response also increases the width of the PSF. Thus, the signal as sampled is coming not only from where the radiometer is pointed, but includes a "memory" of the input from where it had been looking (Green and Wielicki, 1996). If we define x as an imager radiance or cloud property, the weighted average value of x over a CERES footprint is given by:

$$\bar{x} = \frac{\int_{\mathrm{FOV}} P(\delta, \beta) x(\delta, \beta) \cos\delta d\beta d\delta}{\int_{\mathrm{FOV}} P(\delta, \beta) \cos\delta d\beta d\delta} \tag{1}$$

where δ and β are the angular coordinates of a point in the CERES FOV. The PSF $P(\delta, \beta)$ provides the weight assigned to x within the FOV and is defined and discussed in detail in Green and Wielicki (1996) and Smith (1994).

Radiance-to-Flux Conversion

As a scanning radiometer, CERES measures radiances whereas it is radiative fluxes that are needed for scientific investigations. The radiance-to-flux conversion is carried out using empirical ADMs. For a given scene type, an instantaneous flux is inferred from an unfiltered radiance as follows:

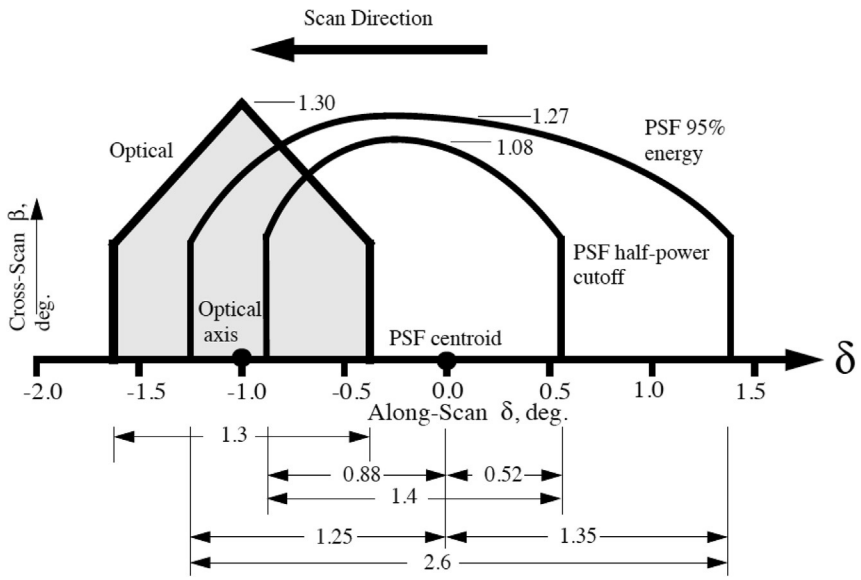

Fig. 7 CERES field-of-view.

$$F(\theta_0) = \frac{\pi I(\theta_0, \theta, \phi)}{R_j(\theta_0, \theta, \phi)} \tag{2}$$

where F is the flux, I is the unfiltered radiance, θ_0 is the solar zenith angle, θ is the viewing zenith angle, and ϕ is the relative azimuth angle between the satellite and solar plane, R_j is the anisotropic factor for scene type j. R provides a measure of how much a given scene type deviates from an isotropic surface ($R=1$) in a particular viewing geometry. A commonly used approach for constructing ADMs is the so-called sorting-into-angular bins method (Suttles et al., 1988), whereby measured radiances are sorted and averaged into discrete angular bins for individual scene types. Ideally, the ADMs are constructed using multiple years of observations acquired over a wide range of viewing geometries. The mean radiances (I) are then integrated over the upwelling hemisphere to produce a mean ADM flux (F). The anisotropic factors (R) for scene type j are then calculated as:

$$R_j(\theta_0, \theta, \phi) = \frac{\pi \hat{I}_j(\theta_0, \theta, \phi)}{\int_0^{2\pi}\int_0^{\pi/2} \hat{I}_j(\theta_0, \theta, \phi)\cos\theta\sin\theta d\theta d\phi} = \frac{\pi \hat{I}_j(\theta_0, \theta, \phi)}{\hat{F}_j(\theta_0, \theta, \phi)}. \tag{3}$$

Prior to CERES, ADMs were developed for the ERBE for 12 scene types (Suttles et al., 1988; Smith et al., 1986) determined using the maximum likelihood estimation technique applied to observed SW and LW radiances (Wielicki and Green, 1989). Following the launch of CERES on TRMM, new ADMs were developed for hundreds of scene types with much improved angular resolution. This is accomplished by using the CERES RAP mode. Another major advance is in scene identification—the CERES ADMs are based upon coincident imager retrievals for scene information within CERES footprints. The variables used to define CERES ADM scene types are selected based upon their influence on anisotropy. They include cloud fraction, cloud optical depth, cloud phase, cloud effective temperature, wind speed, surface type, snow and ice coverage, sea ice brightness, etc. CERES TRMM ADMs were developed using 9 months of CERES and VIRS data (Loeb et al., 2003). This set of ADMs represents a much improved anisotropy characterization compared to those used during ERBE. Loeb et al. (2005) developed ADMs for CERES instruments on Terra and Aqua using cloud properties retrieved from MODIS for scene identification (Minnis et al., 2011). Recently, Su et al. (2015) updated and improved these based upon lessons learned from extensive validation efforts. The Su et al. (2015) ADMs rely on an updated cloud algorithm for scene identification (Edition 4). In addition to using the sorting-into-angular bins method for developing ADMs, the CERES Terra and Aqua ADMs are also derived using analytical functions when appropriate to characterize the anisotropy over some scene types. SW anisotropy is a strong function of θ_0, θ, and ϕ, and therefore the SW ADMs are developed as a function of all these three variables. The LW/WN anisotropy is generally a weak function of θ_0 and ϕ, and thus LW/WN ADMs are developed only as a function of θ. One exception is over clear land where shadowing by vegetation and rough terrain produces a heterogeneous distribution of surface temperatures, resulting in a stronger dependence on ϕ compared to flat surfaces (Minnis, 2004).

Fig. 8A and **B** shows anisotropic factors as a function of viewing zenith angle for liquid water clouds with three $\ln(f\tau)$ values and for different cloud phases with $\ln(f\tau)=6$ (f is the percentage cloud fraction and τ is the cloud optical depth). Here, $\theta_0=44$–46° and ϕ corresponds to the principal plane (forward and back scatting directions correspond to positive and negative viewing zenith angle values, respectively). Anisotropic factors are highly sensitive to $\ln(f\tau)$ within approximately 20 degrees of nadir and at the oblique viewing zenith angles, particularly in the forward scattering direction (**Fig. 8A**). The liquid and mixed clouds exhibit well-defined peaks in anisotropy due to cloud glory and rainbow features, while ice clouds exhibit peaks in anisotropy in the specular reflectance direction (**Fig. 8B**). For cloudy scenes with $\ln(f\tau)=6$, R is about 0.8 for nadir viewing geometry, so by assuming these clouds are isotropic would result in a 20% underestimation in SW flux. Similarly, for an oblique viewing geometry ($\theta=63^\circ$), R is about 1.5. Here the isotropic assumption would lead to a 50% overestimation in SW flux. **Fig. 9** shows an example of LW anisotropic factors over cloudy ocean for thick (solid line) and thin (dashed line) clouds. The LW anisotropic factors decrease as the viewing zenith angle increases, often referred to as limb darkening. LW anisotropy is more pronounced for thinner clouds because the

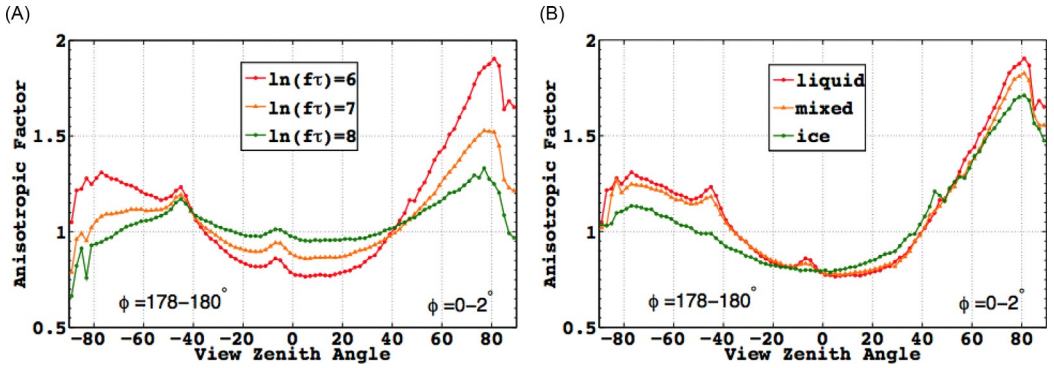

Fig. 8 CERES SW anisotropic factors over ocean in the principle plane for (A) liquid clouds with different $\ln(f\tau)$ values, (B) clouds of different phases with $\ln(f\tau)=6$. Anisotropic factors are derived for $\theta_0=44$–46°.

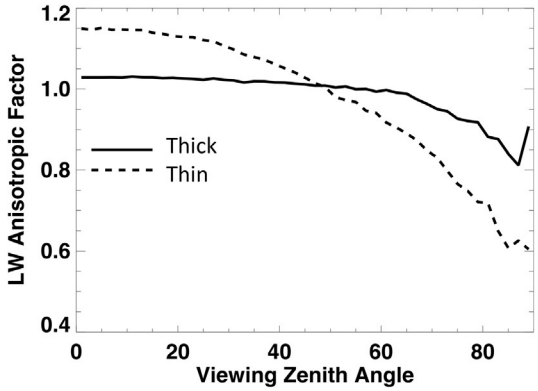

Fig. 9 CERES LW anisotropic factors over ocean for thick clouds *(solid line)* and thin clouds *(thin line)* under overcast conditions.

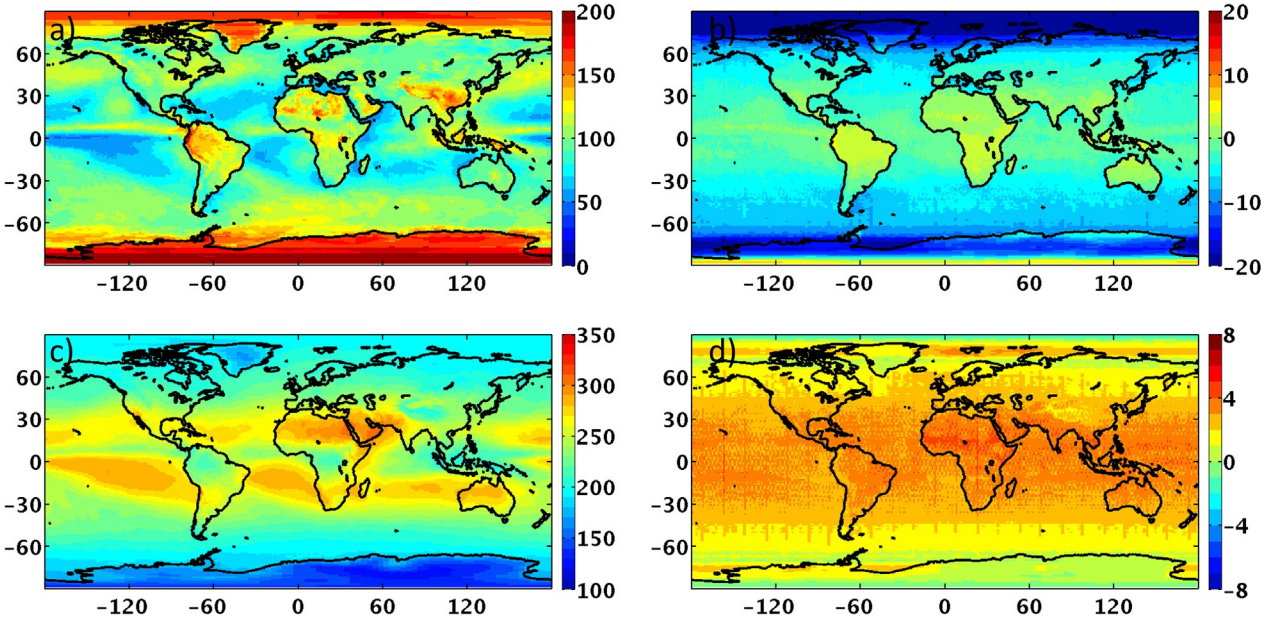

Fig. 10 Annual mean TOA SW flux derived using CERES ADMs (A), annual mean difference between SW flux derived assuming isotropic surfaces and using CERES ADMs (B), (C), and (D) are the same as (A) and (B) but for TOA LW flux.

contribution from the warm ocean surface transmitted through the cloud at nadir is attenuated rapidly with viewing zenith angle. Thicker clouds are opaque to radiation from the surface at all viewing zenith angles. When the cloud-top is in the upper troposphere, there is relatively little attenuation, resulting in a more isotropic ADM.

These examples clearly show that Earth scenes are far from isotropic and without accurate quantification of the unique anisotropic characteristics of each scene type, large errors in the ERB will occur. Fig. 10A and C shows the annual mean TOA SW and LW fluxes derived using the CERES ADMs, respectively, together with the corresponding differences obtained when one assumes the scenes are isotropic (Fig. 10B and D). The annual mean CERES SW flux is 98.9 W m^{-2}. If we use the isotropic assumption, it reduces to 94.8 W m^{-2}. Regionally, reductions of up to 20 W m^{-2} over the polar region and slight increases over the tropical land regions are observed. For LW flux, the annual mean increases from 238.9 to 241.5 W m^{-2} if we use the isotropic assumption. The LW difference is more uniform compared to SW, with the largest positive bias occurring in the Saharan desert. The meridional stripes seen in the LW difference plot are related to the large viewing zenith angles at the edge of the cross-track swaths.

Temporally and Spatially Averaged CERES Data Products

While CERES instruments aboard Terra, Aqua, and S-NPP provide global coverage daily, they do so from a sun-synchronous, near polar, circular orbit. Consequently, if one were to simply globally average the instantaneous SW and LW TOA fluxes, the average

Table 3 Latitude and longitude intervals for CERES equal-area spatial grid

Latitude range (°)	*Latitude interval (°)*	*Longitude interval (°)*
±45	1	1
45–70	1	2
70–80	1	4
80–89	1	8
89–90	1	360

would be incorrect. In that case, Polar regions would receive too much weight in the average relative to their areal coverage and radiative flux changes between CERES observation times would go unaccounted for. To overcome this problem, the CERES TOA fluxes go through a series of steps to produce spatially gridded and time interpolated TOA fluxes (**Fig. 1**). CERES instantaneous TOA fluxes and imager cloud properties from the SSF product are first averaged onto a uniform nested 1° equal-area grid (defined in **Table 3**) and sorted and averaged into hour boxes. These gridded instantaneous properties are provided in the SSF1deg-Hour product. To determine radiative fluxes in hour boxes in which there are no CERES observations, two separate time interpolation approaches are used in CERES processing system. These are briefly discussed in the following sections and a more in-depth description is in Doelling et al. (2013). After the radiative fluxes have been gridded and time interpolated, global averages can be computed that have the correct temporal and spatial weighting.

SSF1deg Stream

Time interpolation for the SSF stream (**Fig. 1**) assumes that scene properties between CERES observations times remain invariant throughout the day. SW TOA fluxes are determined by accounting for albedo changes with solar zenith angle using scene-dependent empirical diurnal models of albedo, or "albedo directional models." The albedo directional models corresponding to the scenes within a given gridbox at the CERES observation time are used together with the observed albedos to determine TOA fluxes during other times of the day or until the next CERES observation time. The CERES directional models are based upon CERES TRMM ADMs for nonpolar regions (Loeb et al., 2003) and CERES Terra ADMs for polar regions (Su et al., 2015). **Fig. 11** shows examples of CERES TRMM albedo directional models for overcast liquid water clouds over ocean. As the clouds become thicker, the directional model becomes progressively flatter, implying a more Lambertian albedo dependence on solar zenith angle. The mean directional model for a given gridbox on a given day is determined from imager scene information within CERES footprints that fall within the gridbox. Albedos in other hour boxes are computed as follows:

$$\alpha(t_i) = \frac{\overline{\alpha}(t_i)}{\overline{\alpha}(t_o)}\alpha(t_o) \tag{4}$$

where $\alpha(t_i)$ is the estimated albedo in hour box t_i, $\alpha(t_o)$ is the observed albedo at the CERES observation time, and $\overline{\alpha}(t_i)$ and $\overline{\alpha}(t_o)$ are the albedo directional models at t_i and t_o, respectively. The SW TOA flux at t_i is determined from:

$$F(t_i) = \alpha(t_i) S_o \cos(\theta_{oi}) \left({}^{R_{se}}/_{R}\right)^2 \tag{5}$$

where S_o is the instantaneous TOA solar irradiance at mean sun-Earth distance, θ_{oi} is the solar zenith angle at t_i, R_{se} is the mean sun-Earth distance, and R is the actual sun-Earth distance on the day of the observation. In CERES processing, S_o varies daily according to observations from the Solar Radiation and Climate Experiment (SORCE) mission (Kopp et al., 2005). The daily mean TOA SW flux is determined by averaging $F(t_i)$ over all hour boxes during the day (including nighttime hours where the SW flux is zero).

The LW TOA fluxes in the SSF Stream are determined using a half-sine fit over land, with a peak at local solar noon and using a constant nightly flux, and linear interpolation over ocean (Young et al., 1998). This methodology of time interpolation is referred to as the CERES-only (CO) temporal interpolation method in Doelling et al. (2013). This approach is similar to what was used in the ERBE temporal averaging algorithm (Young et al., 1998).

SYN1deg Stream

In the SYN1deg stream, five geostationary (GEO) imagers covering all longitudes between 60°S and 60°N are used to enable explicit estimates of TOA fluxes between CERES observation times. In order for the GEO data to be used for this purpose, they undergo a number of processing steps (**Fig. 12**). GEO images are first screened for artifacts (e.g., bad scan lines) using both automated techniques and visual inspection. Next, the GEO radiances are intercalibrated against imager radiances at 0.65 μm. This involves generating linear regressions of coincident ray-matched imager and GEO radiances within $0.5° \times 0.5°$ latitude–longitude regions each month and using the regression slopes to adjust the GEO radiances. Next, a cloud retrieval algorithm is

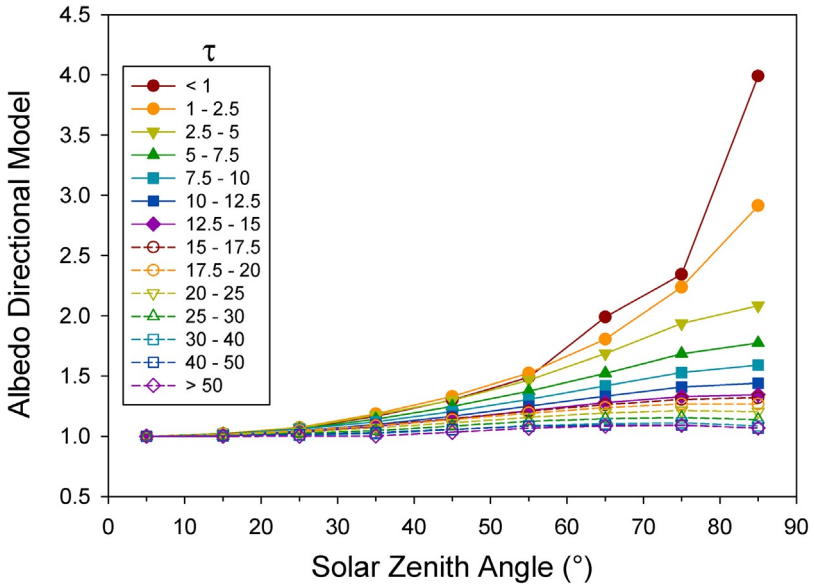

Fig. 11 CERES albedo directional models (diurnal albedo normalized to overhead sun) for overcast liquid water clouds over ocean as a function of cloud optical depth (*t*).

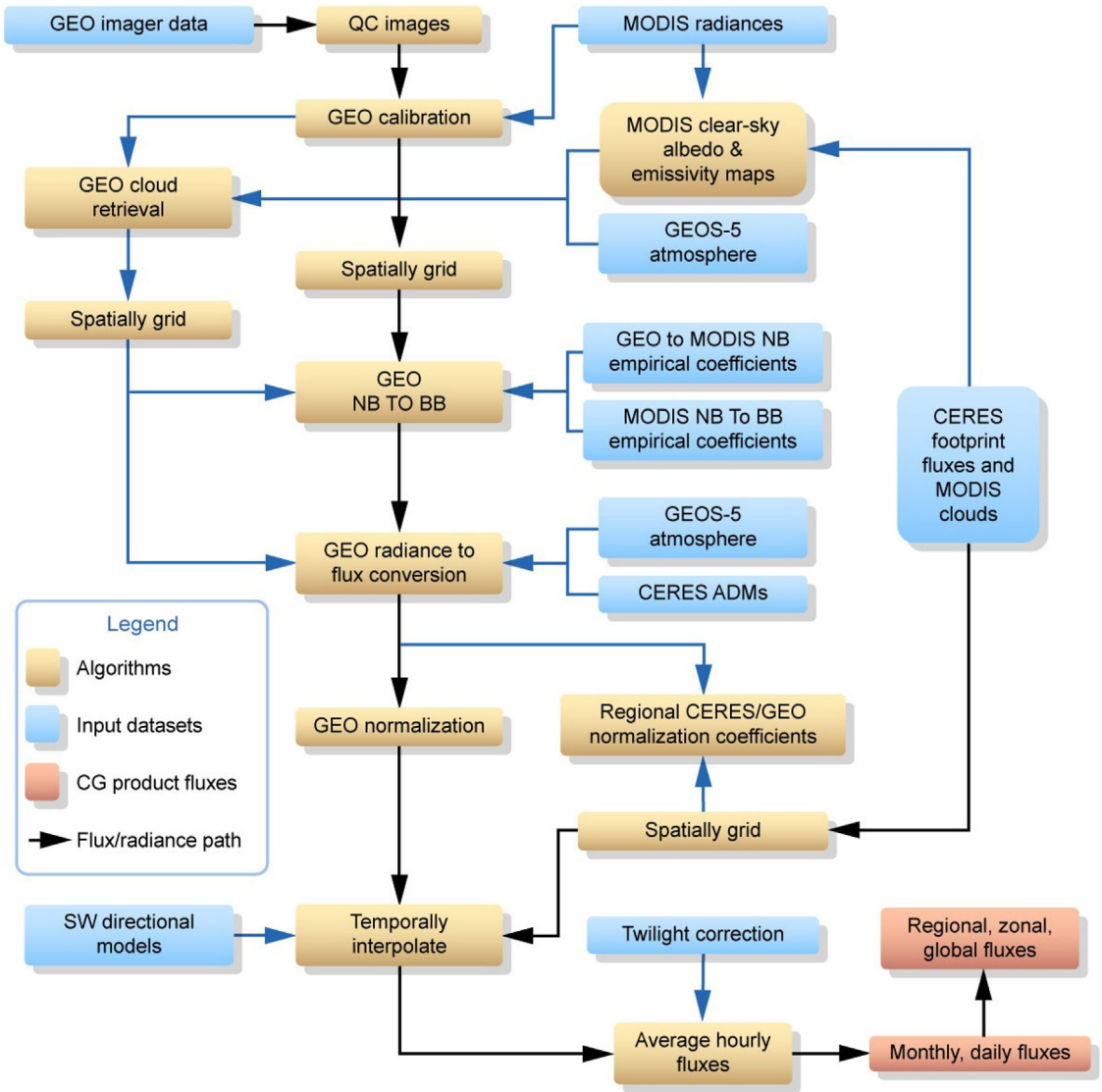

Fig. 12 Flowchart of steps used to produce the CERES SYN1deg product.

used to infer cloud properties from the GEO radiances. The cloud retrieval algorithm applied depends on the available channels. For GEO imagers having no channel at ~3.8 μm, a two channel method (Minnis et al., 1995) is used. Otherwise, the algorithm is similar to that used by the CERES to analyze MODIS and VIIRS (Minnis et al., 2008a, 2011). Next, the GEO narrowband radiances averaged over 1° ×1° latitude–longitude regions are converted to broadband radiative fluxes using empirical narrow-to-broadband radiance and radiance-to-flux algorithms. Finally, the GEO broadband flux estimates are normalized on a region-by-region basis using coincident CERES TOA fluxes. This mitigates GEO artifacts and anchors the GEO calibration to CERES. Using this approach, CERES SYN1deg products incorporate 3-hourly GEO derived fluxes and are produced at 3-hourly, daily, and monthly timescales. We note that Edition 4 uses 1-hourly GEO data to produce 1-hourly, 3-hourly, daily, and monthly output.

Validation

The CERES SSF1deg product provides global coverage daily with excellent calibration stability (Loeb et al., 2012a), but samples only specific times of the day because it relies on CERES data, which are restricted to sun-synchronous satellite orbits. Consequently, regional mean TOA fluxes will be in error over areas with strong diurnal cycles. This is illustrated in **Fig. 13**, which shows annual mean differences in SW TOA flux between CERES Terra SSF1deg and combined CERES Terra–Aqua SYN1deg for the year 2002. In marine stratocumulus regions off the west coasts of North and South America and Africa, SW TOA fluxes from CERES Terra SSF1deg are too high because cloud cover is greater in the morning, when CERES Terra observes these regions. Similarly, SW TOA fluxes from CERES Terra SSF1deg are too low in land convective regions such as South America and Central Africa because land convection typically peaks in the afternoon. By combining the CERES Terra, Aqua and GEO products, SYN1deg provides a far more complete representation of the diurnal cycle compared to SSF1deg, and therefore a more accurate representation of the regional distribution of SW TOA flux. This is further confirmed through comparisons between CERES SYN1deg and observations from the Geostationary Earth radiation budget (GERB) instrument, which provides broadband radiative fluxes between 60°S–60°N centered above the equator at 0° longitude with a time resolution of 15 min. Doelling et al. (2013) shows excellent agreement between CERES SYN1deg and GERB TOA fluxes over a range of cloud conditions.

However, because GEO data are used in SYN1deg, artifacts in the GEO data over certain regions and time periods can cause discontinuities in the CERES record. This is especially true in the early part of the CERES record. While the CERES team attempts to remove most of the GEO derived flux biases by normalizing the fluxes with CERES at Terra or Aqua observation times, spurious jumps in the SW TOA flux can still occur when GEO satellites are replaced due to changes in satellite position, calibration and/or visible sensor spectral response, and imaging schedules. Such artifacts in the GEO data can be problematic in studies of TOA radiation interannual variability and/or trends. As an example, **Fig. 14A** and B shows regional trends in SW TOA flux for CERES SSF1deg-Month Ed3A and SYN1deg-Month Ed3A, respectively, for Mar. 2000–Feb. 2010. While the trend patterns are similar in

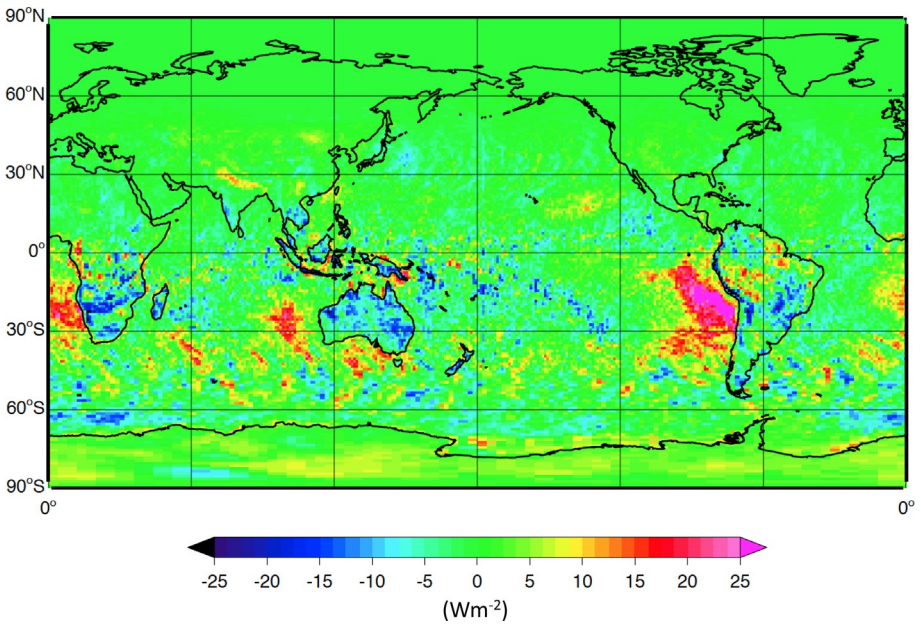

Fig. 13 SW TOA flux difference between SSF1deg-Terra and SYN1deg Ed3a for Jan. 2010.

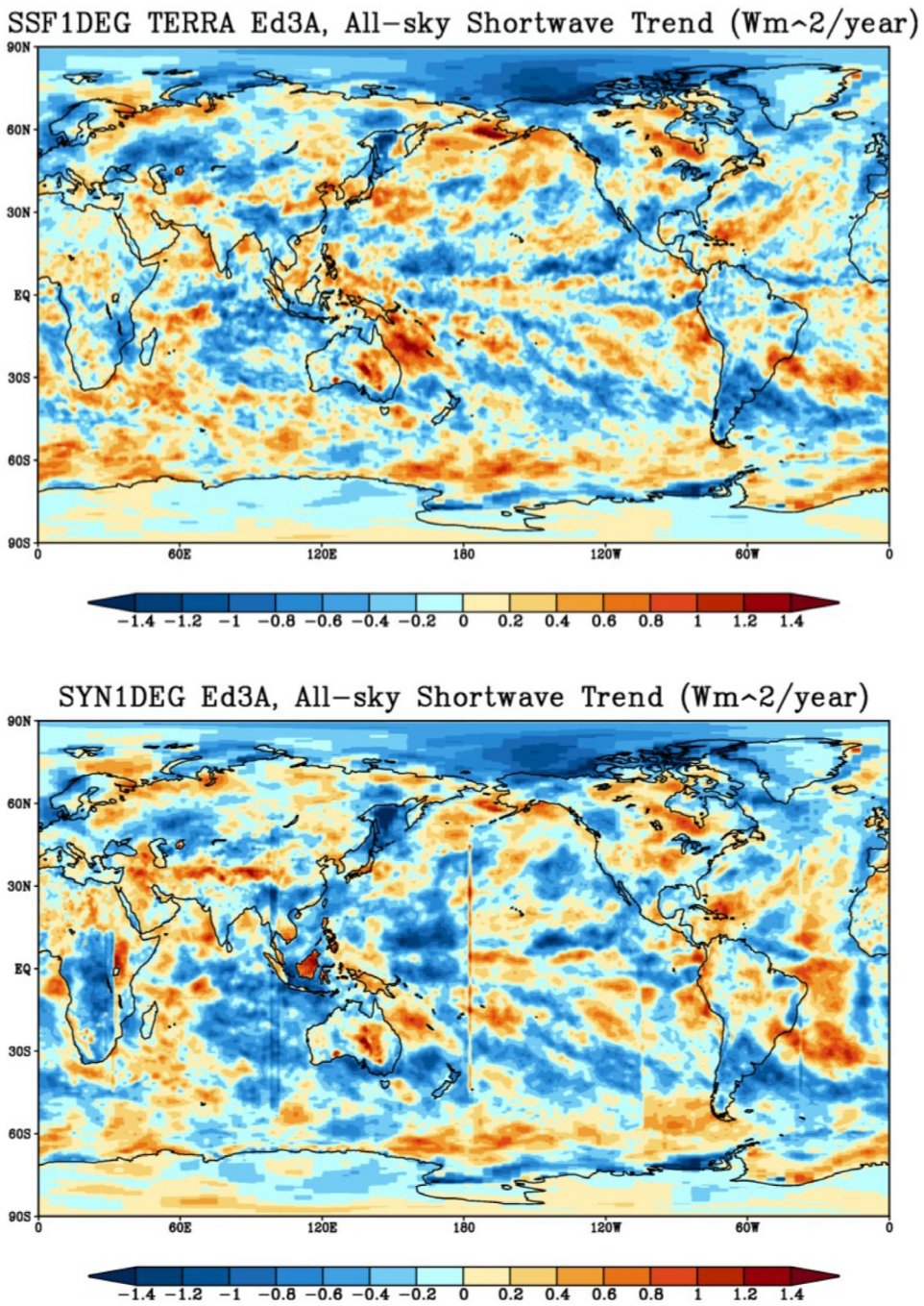

Fig. 14 Regional trends in SW TOA flux (W m^{-2} per year) for Mar. 2000–Feb. 2010 from (A) SSF1deg Ed3A and (B) SYN1deg Ed3A.

Fig. 14A and B, vertical lines corresponding to geostationary satellite boundaries are clearly visible in Fig. 14B near 30°E, 100°E, 180°E, 105°W, and 40°W. The geostationary artifacts are more pronounced over Africa and Asia, but also show up to the east of South America. Similarly, Fig. 15Aand B shows SW TOA flux anomalies for CERES SYN1deg-Month and SSF1deg-Month Ed3A between 60°S–60°N and 110°E–180°E. While the SW TOA flux anomalies appear to track one another closely (Fig. 15A), their difference reveals large discontinuities, particularly when Multifunctional Transport Satellite (MTSAT)-1R replaces Geostationary Operational Environmental Satellite (GOES)-9 in Nov. 2005. A slight blurring effect was observed for the MTSAT-1R imager visible channel, which was mitigated using a pixel PSF correction algorithm (Doelling et al., 2015; Khlopenkov et al., 2015). The correction was included in the SYN1deg Ed4A products.

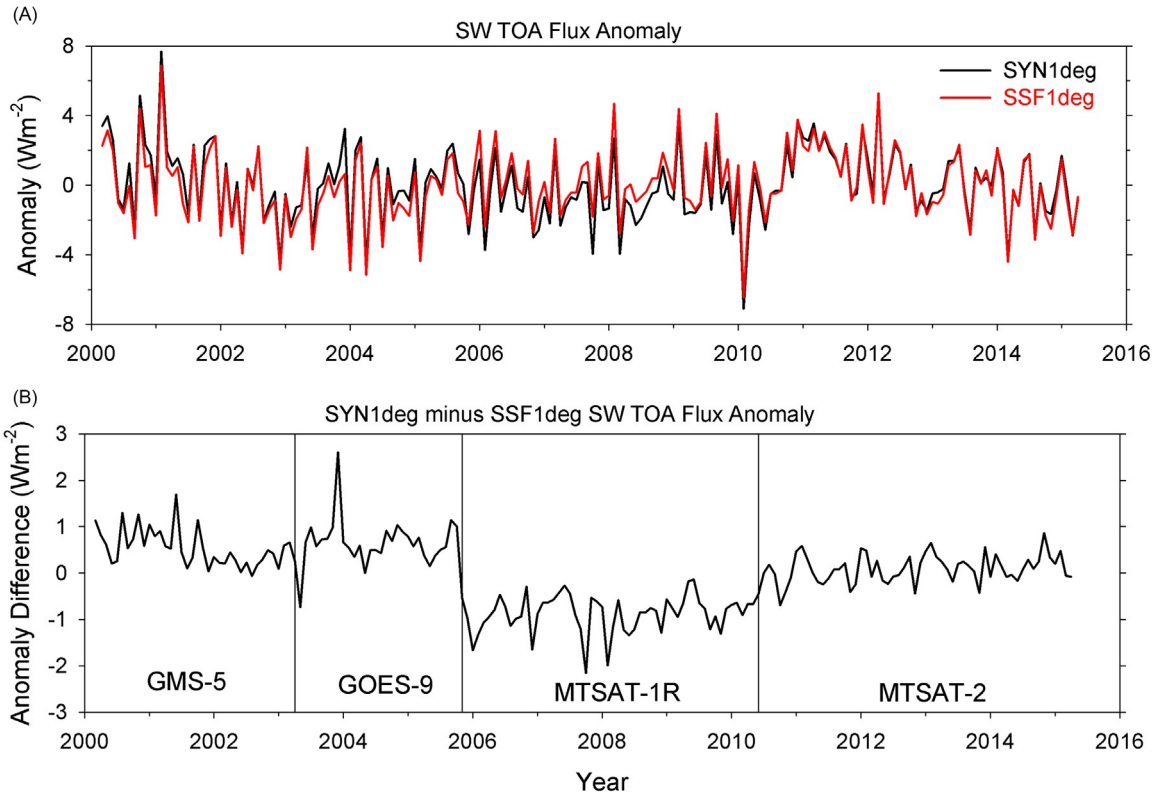

Fig. 15 (A) SW TOA flux anomalies for 60°S–60°N and 110°E–180°E between Mar. 2000 and Apr. 2015. (B) SW TOA flux anomaly difference between SYN1deg and SSF1deg. The CERES data product version is Edition 3.

Thus, by incorporating additional information from geostationary satellite instruments, the CERES SYN1deg data product provides a better representation of the regional distribution of SW TOA flux, but because of GEO artifacts early in the CERES record, spurious jumps are observed when interannual variations are compared with SSF1deg.

Energy Balanced and Filled Product

Despite recent improvements in satellite instrument calibration and the algorithms used to determine CERES SW and LW outgoing TOA radiative fluxes, a sizeable imbalance still persists in the average global net radiation at the TOA (or Earth energy imbalance; EEI). For example, using the most recent CERES Edition 3 Instrument calibration improvements, the SYN1deg_Edition3 net TOA flux imbalance is $\approx$3.4 W m^{-2}, much larger than the expected mean range of $\approx$0.5–1.0 W m^{-2} (von Schuckmann et al., 2016). Constraining the absolute value of EEI from satellite measurements is extremely challenging. EEI is a small residual of incoming and outgoing TOA fluxes that are two orders-of-magnitude larger. Achieving a 50% uncertainty in EEI would require the total outgoing radiation (SW plus LW TOA fluxes) to be known to 0.2 W m^{-2} or 0.06%, roughly an order-of-magnitude more accurate than present-day ERB sensors. The bias in EEI from CERES is problematic in applications that use ERB data for climate model evaluation, estimations of the Earth's annual global mean energy budget, and studies that infer meridional heat transports. Another limitation that is problematic for studies requiring clear-sky TOA fluxes is the presence of data gaps in monthly mean clear-sky TOA flux maps owing to a lack of cloud-free CERES footprints within $1^\circ \times 1^\circ$ regions as identified by imager data. This occurs frequently over the Southern Oceans, North Atlantic Ocean, and Amazon region (Loeb et al., 2009). A third issue, noted in the previous section, is that while the SYN1deg and SSF1deg data products are useful either for providing a good representation of regional mean TOA fluxes or for tracking interannual variations, neither is well suited to address both items.

The goal of CERES Energy Balanced and Filled Product (EBAF) product is to provide clear and all-sky monthly mean TOA fluxes on a $1^\circ \times 1^\circ$ latitude-by-longitude equal-area grid that has a net TOA flux imbalance that is consistent with our best estimate based upon in situ ocean heat content measurements; provides monthly clear-sky TOA fluxes in all regions; and provides a good representation of the regional mean TOA flux distribution while at the same time ensuring that spurious jumps from GEO artifacts do not impact TOA flux interannual variations. In the following sections, we briefly discuss how each of these three items is addressed in the CERES EBAF data product.

Global TOA Net Imbalance

Currently, the most accurate method of determining the EEI is by estimating the rate of change of energy storage in the climate system (Hansen et al., 2011; Trenberth et al., 2014; Church et al., 2011). Approximately 93% of the excess energy in the climate system ends up being stored in the ocean (Bindoff, 2013), the remainder is associated with changes in ice, land, and the atmosphere. Thus, EEI can be inferred from in situ based observations of ocean heating rate obtained from floats measuring vertical temperature profiles in the ocean and estimates of smaller contributions in the atmosphere, land, and cryosphere. The most complete in situ ocean measurements for this purpose is from the Argo network (Gould, 2004), which consists of over 3500 floats sampling temperature and salinity to a depth of 1800 m. Despite the large number of Argo floats, sampling errors still limit reliable estimates of EEI for time scales of less than 5 years. Loeb et al. (2012b) used 5 years of Argo data between Jul. 2005 and Jun. 2010 together with estimates of other energy storage in the system to determine the EEI to be 0.58 ± 0.38 W m^{-2}. They then used an objective constrainment algorithm to make a one-time adjustment to SW and LW TOA fluxes within their ranges of uncertainty in order to anchor the CERES net TOA flux time-series to the Argo-based estimate of EEI (Loeb et al., 2009). The combination of CERES and Argo provides an optimal way of capitalizing on the strengths of satellite and in situ measurements, as the CERES data provide the spatial coverage and radiometric stability required to resolve higher temporal variations in EEI (e.g., interannual), and Argo in situ data enables a more accurate absolute value of EEI.

Clear-Sky TOA Fluxes

In order to significantly reduce the problem of data gaps in monthly mean clear-sky TOA flux maps due to a lack of completely cloud-free CERES footprints within $1^\circ \times 1^\circ$ regions, EBAF gridbox mean clear-sky fluxes are determined using an area-weighted average of CERES broadband fluxes from completely cloud-free footprints and imager-derived "broadband" clear-sky fluxes estimated from the cloud-free portions of CERES footprints with $<$100% cloud cover. In both cases, clear regions are identified using the CERES team's cloud mask applied to imager pixel data (Minnis et al., 2008b; Trepte et al., 2002). Clear-sky fluxes in partly cloudy CERES footprints are derived using imager–CERES narrow-to-broadband regressions to convert the imager narrowband radiances over the clear portions of a footprint to broadband SW radiances. The imager-based "broadband" radiances are converted to radiative fluxes using CERES ADMs ("**Radiance-to-Flux Conversion**" section). A more detailed description of the procedure for inferring clear-sky TOA fluxes in EBAF is provided in Loeb et al. (2009).

TOA Flux Temporal Interpolation

SW TOA flux

To maintain the excellent CERES instrument calibration stability of SSF1deg and also to preserve diurnal information in SYN1deg, EBAF uses a new approach involving scene-dependent diurnal corrections to convert daily regional mean SSF1deg fluxes to diurnally complete values analogous to SYN1deg, but without geostationary artifacts. The diurnal corrections are ratios of SYN1deg-to-SSF1deg fluxes defined for each of the five geostationary satellite domains and each calendar month. They depend upon surface type and MODIS cloud fraction and height retrievals, and thus can vary from one day to the next along with the cloud properties (i.e., they are dynamic). For Mar. 2000–Jun. 2002, TOA fluxes are based upon CERES observations from the Terra spacecraft, while for Jul. 2002 onwards, CERES observations from both Terra and Aqua are utilized in order to improve the accuracy of the diurnal corrections. The diurnal corrections applied to SSF1deg fluxes dramatically improve the EBAF record by minimizing the impact of geostationary satellite artifacts, especially with respect to temporal regional trends.

The uncertainty in $1^\circ \times 1^\circ$ regional SW TOA flux is evaluated separately for Mar. 2000–Jun. 2002 (Terra-Only period) and for Jul. 2002–Dec. 2010 (Terra–Aqua period). To determine uncertainties for the Terra-Only period, we use data from the Terra–Aqua period and compare regional fluxes derived by applying diurnal corrections to the Terra SSF1deg product with regional fluxes determined by averaging fluxes from the Terra and Aqua SYN1deg data products. The SYN1deg products combine CERES observations on Terra or Aqua with five geostationary instruments covering all longitudes between 60°S and 60°N, thus providing the most temporally and spatially complete CERES dataset for Terra or Aqua. For Mar. 2000–Jun. 2002 (Terra-Only period), the overall regional root-mean-square (RMS) error is 4 W m^{-2}. Uncertainties for months when both Terra and Aqua are available (Jul. 2002–Dec. 2010) are determined by comparing regional fluxes derived by applying diurnal corrections to the average of Terra and Aqua SSF1deg fluxes with average Terra and Aqua regional fluxes from SYN1deg. In that case, the regional RMS error decreases to 2.7 W m^{-2}. To place these results into context, the regional RMS difference between Terra and Aqua SYN1deg SW TOA fluxes is 4.4 W m^{-2}.

LW TOA flux

LW TOA fluxes in EBAF are derived directly from the Terra CERES_SYN1deg data product for Mar. 2000–Dec. 2010. In contrast to the SW, geostationary instruments carry onboard calibration sources (blackbodies) to correct for instrument drift in the LW. Consequently, the trend from EBAF falls within 0.1 W m^{-2} per decade of SSF1deg, which only relies on CERES.

Conclusions

The TOA ERB describes the balance between how much solar energy the Earth absorbs and how much terrestrial thermal infrared radiation it emits. The ERB is a critical property of the climate system that is altered both through anthropogenic and natural climate forcings and by substantial internal variability of the climate system acting over a wide range of time-space scales. Consequently, it is critical that we accurately monitor the ERB over multiple decades to enable improved understanding of the processes and changing energy flows occurring within the climate system. ERB data are utilized in many areas of climate research, including climate model evaluation, climate feedback analyses, aerosol radiative forcing determination, energy/water cycle closure, and large scale energy transport analysis.

There is a long heritage of observing the ERB with satellite measurements that dates back to the beginning of the satellite era. Despite this, a continuous long-term global record of the ERB from broadband radiometers designed specifically for this purpose only began at the turn of this century with the launch of the first CERES instrument. Compared to prior ERB missions, the CERES project has made many advances in instrumentation, calibration techniques, and algorithm development and validation. The CERES CDRs account for the regional and global diurnal cycle of radiative fluxes and include coincident cloud, aerosol, surface, and meteorological properties so that changes in the ERB and climate system components can be investigated in an integrated manner. This is accomplished by supplementing CERES observations with data from other instruments either flying alongside CERES (e.g., high-resolution multichannel imagers) or at the same time as CERES (e.g., geostationary instruments). The level of data fusion involved in creating CERES data products is unprecedented. Currently, 13 instruments on eight spacecraft are all integrated to obtain climate accuracy in radiative fluxes from the top to the bottom of the atmosphere.

Thus far, six CERES instruments have flown on four different spacecrafts. CERES Flight Models (FM) 1–5 aboard the Terra, Aqua, and S-NPP spacecrafts continue to collect ERB observations. Plans are under way to launch the final CERES instrument (FM6) on the first Joint Polar Satellite System (JPSS-1) spacecraft in 2017. Efforts are also under way to build a CERES follow-on instrument called the radiation budget instrument that will fly on JPSS-2. The objective is to continue the ERB record that started in 2000 and produce a gap-free 3-decade long dataset for climate research.

References

Arking A and Levine JS (1967) Earth albedo measurements: July 1963 to June 1964. *Journal of the Atmospheric Sciences* 24: 721–724.

Barkstrom BR (1984) The Earth radiation budget experiment (ERBE). *Bulletin of the American Meteorological Society* 65: 1170–1185.

Bindoff NL, Stott PA, AchutaRao KM, et al. (2013) Detection and attribution of climate change: from global to regional. In: Stocker TF, Qin D, Plattner G-K, Tignor M, Allen SK, Boschung J, Nauels A, Xia Y, Bex V, Midgley PM (eds.) *Climate change 2013: the physical science basis. Contribution of working group I to the fifth assessment report of the intergovernmental panel on climate change*, pp. 867–952. Cambridge: Cambridge University.

Church JA, White NJ, Konikow LF, Domingues CM, Cogley JG, Rignot E, Gregory JM, van den Broeke MR, Monaghan AJ, and Velicogna I (2011) Revisiting the Earth's sea-level and energy budgets from 1961 to 2008. *Geophysical Research Letters* 38(18). n/a-n/a.

Doelling DR, Loeb NG, Keyes DF, Nordeen ML, Morstad D, Nguyen C, Wielicki BA, Young DF, and Sun M (2013) Geostationary enhanced temporal interpolation for CERES flux products. *Journal of Atmospheric and Oceanic Technology* 30(6): 1072–1090.

Doelling DR, Khlopenkov KV, Okuyama A, Haney CO, Gopalan A, Scarino BR, Nordeen M, Bhatt R, and Avey LA (2015) MTSAT-1R visible imager point spread correction function, Part I: The need for, validation of, and calibration with. *IEEE Transactions on Geoscience and Remote Sensing* 53(3): 1513–1526.

Gould Jea (2004) Argo profiling floats bring new era of in situ ocean observations. *Eos, Transactions of the American Geophysical Union* 85: 185–191.

Green RN and Wielicki BA (1996) *Clouds and the Earth's Radiant Energy System (CERES) Algorithm Theoretical Basis Document: Convolution of imager cloud properties with CERES footprint point spread function*.

Hansen J, Sato M, Kharecha P, and von Schuckmann K (2011) Earth's energy imbalance and implications. *Atmospheric Chemistry and Physics* 11: 13421–13449.

House FB, Gruber A, Hunt GE, and Mecherikunnel AT (1986) History of satellite missions and measurements of the earth radiation budget (1957–1984). *Reviews of Geophysics* 24: 357–377.

Hsu NC, Tsay S-C, King MD, and Herman JR (2004) Aerosol properties over bright-reflecting source regions. *IEEE Geoscience and Remote Sensing* 42(3): 557–569.

Kato S, Loeb NG, Rose FG, Doelling DR, Rutan DA, Caldwell TE, Yu L, and Weller RA (2013) Surface irradiances consistent with CERES-derived top-of-atmosphere shortwave and longwave irradiances. *Journal of Climate* 26(9): 2719–2740.

Khlopenkov KV, Doelling DR, and Okuyama A (2015) MTSAT-1R visible imager point spread function correction. Part II: Theory. *IEEE Transactions on Geoscience and Remote Sensing* 53(3): 1504–1512.

Kopp G, Lawrence G, and Rottman G (2005) The total irradiance monitor (TIM): Science results. *Solar Physics* 230: 129–139.

Kyle HL (1990) Nimbus-7 earth radiation budget data set and its uses. *Long-Term Monitoring of the Earth's Radiation Budget*, Vol. 1299 *Proc. SPIE, Orlando, FL* p. 27.

Lee RB, Avis LM, Gibson MA, and Kopia LP (1992) Characterizations of the mirror attenuator mosaic—Solar diffuser plate. *Applied Optics* 31(31): 6643–6652.

Lee RB III, Barkstrom BR, Bitting HC, Crommelynck D, Paden J, Pandey DK, Priestley KJ, Smith GL, Thomas S, Thornhill K, and Wilson RS (1998) Prelaunch calibrations of the Clouds and the Earth's Radiant Energy System (CERES) tropical rainfall measuring mission and Earth Observing System morning (EOS-AM1) spacecraft thermistor bolometer sensors. *IEEE Transactions on Geoscience and Remote Sensing* 36(4): 1173–1185.

Levy RC, Remer LA, Mattoo S, Vermote EF, and Kaufman YJ (2007) Second-generation operational algorithm: Retrieval of aerosol properties over land from inversion of Moderate Resolution Imaging Spectroradiometer spectral reflectance. *Journal of Geophysical Research, [Atmospheres]* 112. D13.

Loeb NG, Priestley KJ, Kratz DP, Geier EB, Green RN, Wielicki VA, Hinton RO, and Nolan SK (2001) Determination of unfiltered radiances from the clouds and the Earth's Radiant Energy System instrument. *Journal of Applied Meteorology* 40(4): 822–835.

Loeb NG, Loukachine K, Manalo-Smith N, Wielicki BA, and Young DF (2003) Angular distribution models for top-of-atmosphere radiative flux estimation from the Clouds and the Earth's Radiant Energy System instrument on the Tropical Rainfall Measuring Mission satellite. Part II: Validation. *Journal of Applied Meteorology* 42(12): 1748–1769.

Loeb NG, Kato S, Loukachine K, and Manalo-Smith N (2005) Angular distribution models for top-of-atmosphere radiative flux estimation from the Clouds and the Earth's Radiant Energy System instrument on the Terra satellite. Part I: Methodology. *Journal of Atmospheric and Oceanic Technology* 22(4): 338–351.

Loeb NG, Wielicki BA, Doelling DR, Smith GL, Keyes DF, Kato S, Manalo-Smith N, and Wong T (2009) Toward optimal closure of the Earth's top-of-atmosphere radiation budget. *Journal of Climate* 22(3): 748–766.

Loeb NG, Kato S, Su W, Wong T, Rose FG, Doelling DR, Norris JR, and Huang X (2012a) Advances in understanding top-of-atmosphere radiation variability from satellite observations. *Surveys in Geophysics* 33(3–4): 359–385.

Loeb NG, Lyman JM, Johnson GC, Allan RP, Doelling DR, Wong T, Soden BJ, and Stephens GL (2012b) Observed changes in top-of-the-atmosphere radiation and upper-ocean heating consistent within uncertainty. *Nature Geoscience* 5(2): 110–113.

Minnis P (2004) CERES cloud property retrievals from imagers on TRMM, Terra, and Aqua. In: Schäfer Klaus P, Adolfo Comerón, Carleer Michel R, and Picard Richard H (eds.) *Proceedings of SPIE Vol. 5235 Remote Sensing of Clouds and the Atmosphere VIII*. Bellingham, WA: SPIE. http://dx.doi.org/10.1117/12.511210. 0277-786X/04/$15.

Minnis P, Smith WL Jr, Garber DP, Ayers JK, and Doelling DR (1995) Cloud properties derived from GOES-7 for the Spring 1994 ARM Intensive Observing Period using Version 1.0.0 of the ARM satellite data analysis program. *NASA Reference Publication 1366*, 59 p. Hampton VA: NASA Langley Research Center.

Minnis P, Nguyen L, Palikonda R, Heck PW, Spangenberg DA, Doelling DR, Ayers JK, Smith WLJ, Khaiyer MM, Trepte QZ, Avey LA, Chang F-L, Yost CR, Chee TL, and Sun-Mack S (2008a) Near-real time cloud retrievals from operational and research meteorological satellites. *In: vol. 7107-2, Proc. SPIE Remote Sens.Clouds Atmos. XIII, Cardiff, Wales, UK, 15–18 September, 2008; Cardiff, Wales, UK* 8pp.

Minnis P, Trepte QZ, Sun-Mack S, Chen Y, Doelling DR, Young DF, Spangenberg DA, Miller WF, Wielicki BA, Brown RR, Gibson SC, and Geier EB (2008b) Cloud detection in nonpolar regions for CERES using TRMM/VIRS and Terra and Aqua MODIS data. *IEEE Transactions on Geoscience and Remote Sensing* 46: 3857–3884.

Minnis P, Sun-Mack S, Trepte QZ, Chang F-L, Heck PW, Chen Y, Yi Y, Arduini RF, Ayers K, Bedka K, Bedka S, Brown R, Gibson S, Heckert E, Hong G, Jin Z, Palikonda R, Smith R, Smith WL Jr, Spangenberg DA, Yang P, Yost CR, and Xie Y (2010) CERES Edition 3 cloud retrievals. In: *AMS 13th Conf. Atmospheric Radiation, Portland, OR*, pp. 7.

Minnis P, Sun-Mack S, Young DF, Heck PW, Garber DP, Chen Y, Spangenberg DA, Arduini RF, Trepte QZ, Smith WL, Ayers JK, Gibson SC, Miller WF, Chakrapani V, Takano Y, Liou K-N, Xie Y, and Yang P (2011) CERES Edition-2 cloud property retrievals using TRMM VIRS and Terra and Aqua MODIS data, Part I: Algorithms. *IEEE Transactions on Geoscience and Remote Sensing* 49(11): 4374–4400.

Priestley KJ, Barkstrom BR, Lee RB, Green RN, Thomas S, Wilson RS, Spence PL, Paden J, Pandey DK, and Al-Hajjah A (2000) Postlaunch radiometric validation of the Clouds and the Earth's Radiant Energy System (CERES) Proto-flight Model on the Tropical Rainfall Measuring Mission (TRMM) spacecraft through 1999. *Journal of Applied Meteorology* 39(12): 2249–2258.

Priestley KJ, Smith GL, Thomas S, Cooper D, Lee RB, Walikainen D, Hess P, Szewczyk ZP, and Wilson R (2011) Radiometric performance of the CERES Earth Radiation Budget Climate Record Sensors on the EOS Aqua and Terra Spacecraft through April 2007. *Journal of Atmospheric and Oceanic Technology* 28(1): 3–21.

Raschke E and Bandeen WR (1970) The radiation balance of the planet Earth from radiation measurements of the satellite Nimbus II. *Journal of Applied Meteorology* 9: 215–238.

Raschke E, Vonder Haar TH, Bandeen WR, and Pasternak M (1973) The annual radiation balance of the earth-atmosphere system during 1969–70 from Nimbus-3 measurements. *Journal of the Atmospheric Sciences* 30: 341–364.

Remer LA, Kleidman RG, Levy RC, Kaufman YJ, Tanré D, Mattoo S, Martins JV, Ichoku C, Koren I, Yu H, and Holben BN (2008) Global aerosol climatology from the MODIS satellite sensors. *Journal of Geophysical Research* 113: D14.

Rose FG, Rutan DA, Charlock T, Smith GL, and Kato S (2013) An algorithm for the constraining of radiative transfer calculations to CERES-observed broadband top-of-atmosphere irradiance. *Journal of Atmospheric and Oceanic Technology* 30(6): 1091–1106.

Rutan DA, Kato S, Doelling DR, Rose FG, Nguyen LT, Caldwell TE, and Loeb NG (2015) CERES synoptic product: Methodology and validation of surface radiant flux. *Journal of Atmospheric and Oceanic Technology* 32(6): 1121–1143.

Shankar M, Thomas S, and Priestley K (2010) Pre-launch characterization of spectral response functions for the Clouds and Earth's radiant energy system (CERES) instrument sensors. In: Butler JJ, Xiong X, and Gu X (eds.) *Earth Observing Systems Xv*, vol. 7807.

Smith GL (1994) Effects of time response on the point spread function of a scanning radiometer. *Applied Optics* 33(30): 7031–7037.

Smith GL, Green RN, Raschke E, Avis LM, Suttles JT, Wielicki BA, and Davies R (1986) Inversion methods for satellite studies of the Earth's radiation budget: Development of algorithms for the ERBE Mission. *Reviews of Geophysics* 24: 407–421.

Stubenrauch CJ, Rossow WB, Kinne S, Ackerman S, Cesana G, Chepfer H, Di Girolamo L, Getzewich B, Guignard A, Heidinger A, Maddux BC, Menzel WP, Minnis P, Pearl C, Platnick S, Poulsen C, Riedi J, Sun-Mack S, Walther A, Winker D, Zeng S, and Zhao G (2013) Assessment of Global Cloud Datasets from Satellites: Project and Database initiated by the GEWEX radiation panel. *Bulletin of the American Meteorological Society* 94(7): 1031–1049.

Su W, Corbett J, Eitzen Z, and Liang L (2015) Next-generation angular distribution models for top-of-atmosphere radiative flux calculation from CERES instruments: Methodology. *Atmospheric Measurement Techniques* 8(3): 611–632.

Sun-Mack S, Minnis P, Chen Y, Kato S, Yi Y, Gibson SC, Heck PW, and Winker DM (2014) Regional apparent boundary layer lapse rates determined fromCALIPSOand MODIS data for cloud-height determination. *Journal of Applied Meteorology and Climatology* 53(4): 990–1011.

Suttles JT, Green RNG, Minnis P, Smith GL, Staylor WF, Wielicki BA, Walker IJ, Young DF, Taylor VR, and Stowe LL (1988) *Angular radiation models for Earth-atmosphere system: Volume I—Shortwave radiation*.

Taylor R and Stowe LL (1984) Reflectance characteristics of uniform Earth and cloud surface derived from Nimbus 7 ERB. *Journal of Geophysical Research* 89: 4987–4996.

Trenberth KE, Fasullo JT, and Balmaseda MA (2014) Earth's energy imbalance. *Journal of Climate* 27(9): 3129–3144.

Trepte Q, Minnis P, and Arduini RF (2002) Daytime and nighttime polar cloud and snow identification using MODIS data. *In: vol. 4891 Proc. SPIE 3rd Intl. Asia-Pacific Environ. Remote Sens. Symp., Hangzhou, China*, pp. 449–459.

von Schuckmann K, Palmer MD, Trenberth KE, Cazenave A, Chambers D, Champollion N, Hansen J, Josey SA, Loeb N, Mathieu P-P, Meyssignac B, and Wild M (2016) An imperative to monitor Earth's energy imbalance. *Nature Climate Change* 6: 138–144.

Weinstein M and Suomi VE (1961) Analysis of satellite infrared radiation measurements on a synoptic scale. *Monthly Weather Review* 89: 419–428.

Wielicki BA and Green RN (1989) Cloud identification for ERBE Radiative Flux Retrieval. *Journal of Applied Meteorology* 28(11): 1133–1146.

Wielicki B, Barkstom BR, Harrison EF, Lee Iii RB, Smith GL, and Cooper J (1996) Clouds and the Earth's Radiant Energy System (CERES): An Earth Observing System Experiment. *Bulletin of the American Meteorological Society* 77: 853–868.

Young DF, Minnis P, Gibson GG, Doelling DR, and Wong T (1998) Temporal interpolation methods for the clouds and Earth's Radiant Energy System (CERES) Experiment. *Journal of Applied Meteorology* 37: 572–590.